ACS OMEGA

http://pubs.acs.org/journal/acsodf

Article

Do HOMO–LUMO Energy Levels and Band Gaps Provide Sufficient Understanding of Dye-Sensitizer Activity Trends for Water Purification?

Jeffrey Roshan De Lile, Sung Gu Kang, Young-A Son, and Seung Geol Lee*

Cite This: *ACS Omega* 2020, 5, 15052–15062

Read Online

ACCESS | Metrics & More | Article Recommendations | Supporting Information

ABSTRACT: A dye-sensitized solar cell assembly can be used to harvest solar energy, while suitable dye sensitizers can be used to purify water. Here, we characterized the activity trends of four dye sensitizers, namely, PORPC-1, PORPC-2, PORPC-3, and PORPC-4, for water purification applications using density functional theory (DFT) with the Perdew–Burke–Ernzerhof (PBE), B3LYP, and PBE0 functionals, ΔSCF, time-dependent DFT (TD-DFT), and quasiparticle Green's function (*GW*) methods. The energy levels of the highest occupied molecular orbitals (HOMOs) and lowest unoccupied molecular orbitals (LUMOs) were calculated using gas-phase and aqueous-phase methods in order to understand charge-injection abilities and the dye regeneration processes. PBE, B3LYP, PBE0, and TD-DFT methods failed to predict PORPC-4 to be the best sensitizer, while PORPC-2 and PORPC-4 were predicted to be the best sensitizers using ΔSCF coupled with the implicit solvation method, and HOMO–LUMO energies were corrected for the aqueous environment in the *GW* calculations. However, none of these methods accurately predicted the performance trend of all four dye sensitizers. Consequently, we used the aggregation assembly patterns of the dye molecules in an aqueous environment to further probe the activity trends and found that PORPC-3 and PORPC-4 prefer *J*-aggregated assembly patterns, whereas PROPC-1 and PORPC-2 prefer to be *H*-aggregated. Therefore, the performance of these dye molecules can be determined by combining HOMO–LUMO energy levels with aggregate-assembly patterns, with the activity trend predicted to be PORPC-4 > PORPC-2 > PORPC-3 > PORPC-1, which is in good agreement with experimental findings.

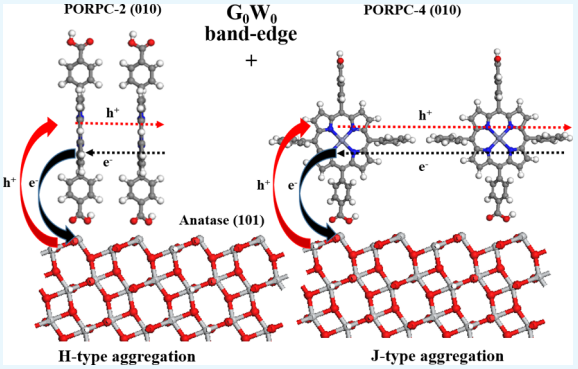

1. INTRODUCTION

The human race faces three major challenges resulting from the unprecedented growth of the world population, namely, finding sustainable energy sources that avoid the problems associated with fossil fuels, engineering crops that yield large quantities of food, and providing clean drinking water.[1−3] Solar energy is considered as the best "green" renewable energy source due to the long lifetime of the sun.[4] The efficient harvesting of solar energy, in principle, can mitigate the global energy crisis, as it exceeds global energy demand.[5,6] Conventional solar cells (photovoltaic technology) and dye-sensitized solar cells are the most popular technologies for harvesting the solar energy associated with solar photons.[6−10] These technologies provide feasible solutions for sustainable clean energy production and storage. The solar energy stored in photons can be used to drive chemical reactions (i.e., photocatalysis) and can also be effectively used to clean water by removing organic and inorganic pollutants.[11,12] Therefore, solar energy not only provides a solution to the energy problem but also facilitates the purification of water. Although a number of researchers have focused on various semiconductors for photocatalysis, TiO_2 (anatase) has been the most popular choice due to its low toxicity, stability in aqueous environments due to its large band gap, and its low cost.[13−16] However, anatase TiO_2 absorbs solar radiation in the UV region of the solar spectrum (<400 nm), which significantly limit its efficiency.[17,18]

Photocatalysis closely follows the natural photosynthesis process, that is, harvesting light to synthesize food from carbon dioxide and water using the green chlorophyll pigment in green plants and some other microorganisms.[19,20] Hence, it provides a natural laboratory to investigate nature's secrets in the light-harvesting process, in which chlorophyll molecules absorb light and create excitons (electron–hole pairs). These excitons are then transferred to the reaction center where exciton charge-

Received: February 27, 2020
Accepted: May 19, 2020
Published: May 29, 2020

https://dx.doi.org/10.1021/acsomega.0c00870
ACS Omega 2020, 5, 15052–15062

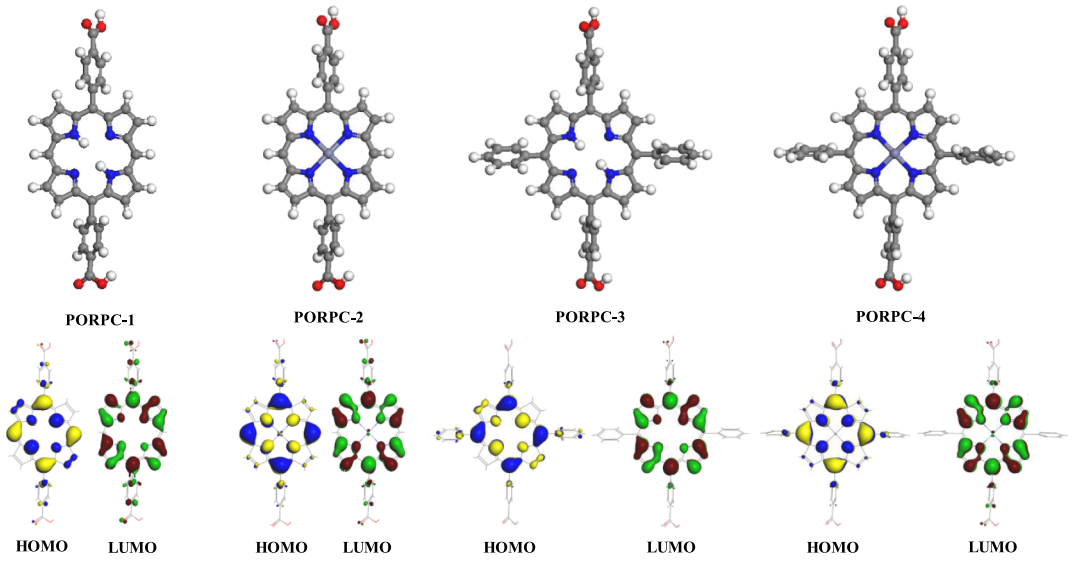

Figure 1. Model structures of the dye sensitizers (upper) and their corresponding HOMOs and LUMOs (lower). Color scheme: carbon, hydrogen, nitrogen, oxygen, and zinc are gray, white, blue, red, and light blue, respectively. HOMOs are shown in yellow and blue, while LUMOs are shown in green and brown.

separation occurs.[21,22] The chlorophyll molecule consists of a β-substituted porphyrin structure with Mg^{2+} chelated in the core region.[23] The adsorption of porphyrin-based sensitizers on the TiO_2 surface has been shown to enhance photocatalytic efficiency due to the absorption of visible-light photons.[24] Therefore, porphyrin and its derivatives have been widely reported as sensitizers that mimic the natural photosensitizing processes of plants.[25,26]

The rational design of dye sensitizers from first-principles-based methods has recently become popular. The development of more-sophisticated functionals that correct for the spurious self-energy of electrons has contributed to the success of computationally designed sensitizers.[27−30] However, computational studies have mainly focused on band gap predictions, frontier molecular orbital positions in the gas phase, and simulating absorption spectra as a means of comparing computations with experimental work.[31−33] Smaller band gap values are believed to improve the absorption of visible-light photons;[28] nevertheless, accurately knowing the positions of the frontier molecular orbitals of the sensitizer with respect to the band edges of TiO_2 is of utmost importance for predicting sensitizer performance. This requirement is particularly critical when predicting sensitizer performance for water-purification applications, as the system must be immersed in water.[34] Consequently, gas-phase calculations are not suitable for predicting the highest occupied molecular orbital (HOMO) and lowest unoccupied molecular orbital (LUMO) energies under such conditions. Implicit solvation methods, such as the conductor-like screening model (COSMO),[35−37] can be used to simulate HOMO−LUMO shifts that result from interactions between water and a dye sensitizer. The aggregation pattern of the photosensitizing dye molecule also plays a crucial role in an aqueous medium. Face-to-face or edge-to-edge aggregation assemblies provide noticeably different photocatalytic performances.[38]

In this work, we used density functional theory (DFT) to study four porphyrin-derived dye sensitizers containing Zn, as well as the corresponding metal-free complexes, using standard semilocal functionals, hybrid functionals, time-dependent DFT (TD-DFT), and quasiparticle-based Green's function (G_0W_0) method. The COSMO implicit solvation model with semilocal and hybrid functional approaches was used. According to our knowledge, ionization potentials (IPs) and electron affinities (EAs) obtained from the G_0W_0 method have not been used to align corrected band edges under aqueous conditions in order to predict the various orientations of dye sensitizers on the anatase(101) surface. Hence, we investigated gas-phase and solvated HOMO−LUMO energies across several different levels of theories in order to understand how solvation affects and shifts the frontier orbitals. In addition, we also studied the assembly patterns of aggregated dye molecules in water, as they have been reported to significantly influence charge transfer.[38] Our calculated results were verified by comparing them with the experimental activity trends of these dye molecules.

2. COMPUTATIONAL METHODS

We studied four porphyrins functionalized with benzoic acid and phenyl groups at their *meso* positions. All functionalized structures contain benzoic acid moieties at opposite ends of their porphyrin frameworks. Among them, two are metal-free and the other two have coordinated Zn ions. Two structures are functionalized with phenyl groups at opposite meso positions, in addition to the benzoic acid units. To avoid any ambiguity, in this work, we refer to these compounds by the same names as those previously used by Min et al.[39] in their experimental work; that is, 4,4′-(porphyrin-5,15-diyl)dibenzoic acid, zinc 4,4′-(porphyrin-5,15-diyl)dibenzoic acid, 4,4′-(10,20-bis(3,5-di-*tert*-butylphenyl)porphyrin-5,15-diyl)-dibenzoic acid, and zinc dimethyl 4,4′-(10,20-bis(3,5-di-*tert*-butylphenyl)porphyrin-5,15-diyl)dibenzoic acid are referred to as PORPC-1, PORPC-2, PORPC-3, and PORPC-4, respectively. Although Min and co-workers[39] used phenyl groups that were modified with di-*tert*-butyl substituents, we omitted these (di-*tert*-butyl) groups for computational convenience. All structures are shown in Figure 1, with the calculated lattice constants summarized in Table 1.

DFT[40,41] with the Perdew−Burke−Ernzerhof (PBE) semilocal exchange−correlation functional[42,43] and the B3LYP

https://dx.doi.org/10.1021/acsomega.0c00870
ACS Omega 2020, 5, 15052−15062

Table 1. Computed Lattice Parameters for the Dye Sensitizers in This Study[a]

	lattice parameters (Å)		
	a	*b*	*c*
PORPC-1	12.70	22.71	6.45
PORPC-2	11.35	22.24	4.96
PORPC-3	21.01	22.65	5.69
PORPC-4	20.07	22.32	5.45
PORPC-MOF	23.96	23.96	6.75

[a]Values for the PORPC-3- and PORPC-4-based MOF are taken from ref 68.

hybrid functional[44−46] was used as implemented in the DMol3 software[47−50] in the Materials Studio suite of programs.[51] Core elements were treated with all-electron pseudopotentials and the DNP basis set using basis set file 4.4. The SCF tolerance level was set to "fine" (10^{-6} Ha). Spin polarization was tested and found not to influence the ground states. Forces were minimized to below 0.002 Ha/Å during optimization. Periodic boundary conditions and symmetry were switched off when studying these dye molecules; this approach is justified as the HOMOs and the LUMOs are only constructed to determine the energy levels of the molecular orbitals as opposed to the band-edge levels of semiconductors. The influence of water was included using the COSMO conductor-like screening model as implemented in the DMol3 code.[52] TD-DFT calculations were also executed within the DMol3 code using the initial B3LYP-optimized ground states.[50] The random-phase approximation (RPA) was then used to calculate the first 25 lowest-energy singlet excitations.[50] Moreover, we used the generalized gradient approximation (GGA) with the PBE-optimized ground states of the dye molecules to study vertical IPs and EAs. To that end, each ground-state structure was doped with an extra electron by setting the charge to −1 (the charge was set to +1 when calculating the IP) and single-point calculations were used to obtain EAs, after which each IP and EA was calculated as follows[53]

$$\mathrm{IP} = (E^0 - E^{+1}) \tag{1a}$$

$$\mathrm{EA} = (E^{-1} - E^0) \tag{1b}$$

where E^0 is the ground-state energy of the dye molecule, E^{-1} is the energy of the negatively charged ion of the dye molecule in the ground state geometry, and E^{+1} is the energy of the positively charged ion of the dye molecule in the ground-state geometry. Therefore, the band gap is conveniently obtained as the difference between the IP and EA. This procedure was repeated with COSMO to study IPs and EAs under aqueous conditions.

Furthermore, the periodic structures of the four dye molecules were simulated using the Vienna Ab initio Simulation Package.[54,55] The projector-augmented-wave (PAW) potential was used to describe the core electrons with a 650 eV plane-wave basis-set cut-off energy.[56] The GGA level of theory with the PBE exchange−correlation functional[42,43] was employed during the initial structural relaxations. Because of the large size of the supercell, a gamma-centered 3 × 3 × 3 grid was used for *k*-point sampling.[57] These GGA−PBE-calculated wavefunctions were then used to set up the hybrid-level PBE0 calculations with the "tight" criterion for the allowed errors in the total orbital energies.[58] Here, we used 30% exact exchange in the PBE0 calculations, as the band gaps of anatase and brookite were accurately reproduced with 30% exact exchange in our previous work.[59] We examined the frontier orbitals and gaps of both relaxed and unrelaxed structures, but no significant differences were observed. In addition, the band-edge positions of the (010) surfaces of the dye molecules were simulated with the PBE0 functional. These calculations were initialized using the wavefunctions saved from the PBE0 bulk-structure optimizations. We calculated quasiparticle energies for these dye molecules using single-shot G_0W_0 using the two-step procedure.[60,61] The PBE- and PBE0-calculated wavefunctions were employed as starting points for the G_0W_0 calculations. The PBE0 starting point may be beneficial because the GGA−PBE functional is known to invert the valence and conduction bands of some materials that contain shallow d-bands.[62] Because of the well-known basis-set incompleteness problem,[63] we checked our calculations using a large number of empty bands (from 176 to 10,032) and *GW* basis-set cutoff values of 100, 150, and 200 eV. Moreover, the plane-wave basis set cutoff was adjusted from 650 to 400 eV to reduce computational cost during the G_0W_0 calculations. Because of the large sizes of the PORPC-3 and PORPC-4 supercells, calculations using a *GW* basis-set cutoff value of 200 eV did not converge due to memory problems. The spectral method was also not used in order to save memory. The number of frequency grid points and number of grid points on which densities of states were evaluated were set to default values throughout these calculations. The complex shift in the Kramers−Kronig transformation was assigned to 0.1, as in the linear-response calculations.[64]

In order to understand the orientation of the aggregate assembly (face-to-face or edge-to-edge), we studied the periodic bulk supercell structures of all dye molecules using DMol3 with the PBE functional and COSMO. The calculated value of the *c*-lattice parameter for each system was used to set the distance between neighboring dye molecules. As we were mainly interested in the (010) surface orientation, dye molecules were arranged such that the benzoic acid groups were vertically oriented, and the face-to-face and the edge-to-edge assemblies were electronically optimized to determine the minimum-energy assembly pattern. Finally, three different surface supercells were generated along the [010], [110], and [100] directions and optimized using the GGA−PBE exchange−correlation functional. A LOCPOT file was generated during these calculations to obtain the surface-dependent potential step ($\Delta V(hkl)$), as described by Stevanović et al.[34] and Kang et al.;[65] these potential steps were used to evaluate the surface-dependent band-edge positions. In our work, we used the method initially described by Kang et al.,[65] to calculate IPs and EAs from the potential step, using

$$\mathrm{IP} = \Delta V(hkl) - [\mathrm{HOMO}_{\mathrm{bulk}}^{\mathrm{DFT}} + \Delta\mathrm{HOMO} - V_{\mathrm{core}}^{\mathrm{bulk}}] \tag{2a}$$

$$\mathrm{EA} = \Delta V(hkl) - [\mathrm{LUMO}_{\mathrm{bulk}}^{\mathrm{DFT}} + \Delta\mathrm{LUMO} - V_{\mathrm{core}}^{\mathrm{bulk}}] \tag{2b}$$

where $\Delta V(hkl)$ is the surface-orientation-dependent potential step, $\mathrm{HOMO}_{\mathrm{bulk}}^{\mathrm{DFT}}$ and $\mathrm{LUMO}_{\mathrm{bulk}}^{\mathrm{DFT}}$ are the GGA−PBE-level bulk HOMO and LUMO energies, respectively. ΔHOMO (ΔLUMO) is the difference between the *GW*-calculated HOMO (LUMO) and the DFT-calculated HOMO (LUMO), while $V_{\mathrm{core}}^{\mathrm{bulk}}$ is the mean electrostatic potential in

https://dx.doi.org/10.1021/acsomega.0c00870
ACS Omega 2020, 5, 15052−15062

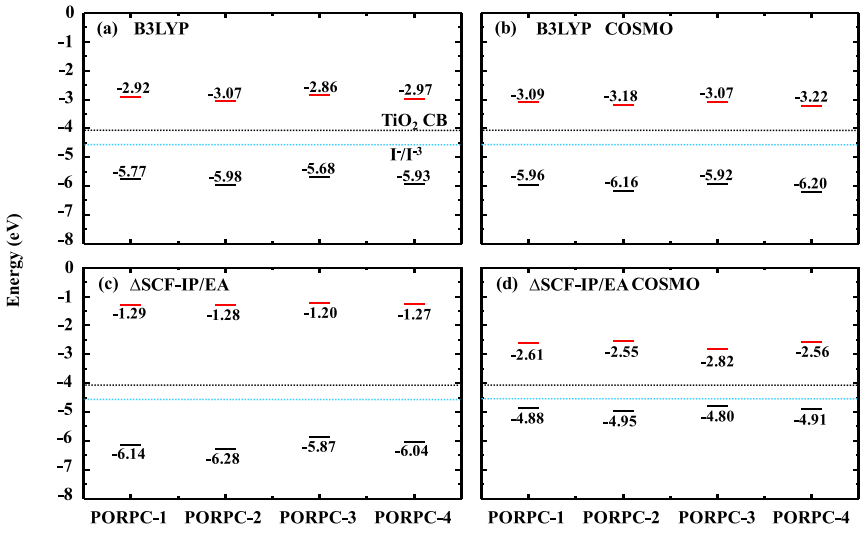

Figure 2. Hybrid B3LYP-functional and ΔSCF HOMO−LUMO levels calculated in (a,c) the gas phase and (b,d) using the solvation model. LUMO levels are shown in red, while HOMO levels are shown in black. The black-dotted line shows the anatase conduction-band minimum; however, for convenience we refer to this as "CB". The blue dotted line corresponds to the iodide-triiodide redox potential.

the bulk. Surface-dependent band-edge calculation details are reported elsewhere.[34,65]

3. RESULTS AND DISCUSSION

3.1. Model Structures. The HOMOs and LUMOs of the dye molecules are displayed in Figure 1, which reveals that the HOMO of each dye molecule is localized on the carbon and nitrogen atoms of the porphyrin framework. The LUMOs are also concentrated on the porphyrin framework, with little delocalization. Although the benzoic acid moieties in the PORPC-3 and the PORPC-4 sensitizers contribute to both the HOMOs and the LUMOs, the phenyl substitutions contribute only to the HOMOs. Interestingly, the Zn ion in the phenyl-substituted PORPC-4 dye molecule does not contribute to the HOMO, which indicates that phenyl substitution significantly depletes charge on the Zn ion. Moreover, the metal−organic framework (MOF) prepared using PORPC-4 monomer units exhibited localized HOMO and LUMO, which lends credence to this work.[66] Because of the lack of explicit crystallographic and morphological information for these molecules, we compared the lattice parameters calculated by us for these dye complexes with the calculated (UFF4MOF force field[67]) lattice parameters of the MOF created from PORPC-3 and PORPC-4.[68] The MOF lattice values are slightly larger than our optimized lattice constants due to the higher dispersion and crystallinity of the MOF. However, the lattice constants were observed to decrease slightly when Zn was introduced into the dye molecule, which is in agreement with experimental observations.[66] Nevertheless, the HOMO and the LUMO energies are more sensitive to the quantum chemical treatment (functionals, methods) than the lattice parameters. Hence, the calculated lattice constants are qualitatively sufficient for our work. Zhou et al.[66] claimed that the *c*-lattice constant provides indirect evidence of the ability of the PORPC-3 and PORPC-4 MOF to transfer charge between neighboring molecules. Consequently, a larger c-lattice parameter is associated with weaker charge transfer between molecules. Based on our calculated lattice parameters, we assume that PORPC-2 and PORPC-4 can effectively transfer charges due to their small c-lattice constants, which is in good agreement with the experimental results of Min et al.,[39] who found that PORPC-2 and PORPC-4 are better sensitizers than PORPC-3 and PORPC-1.

3.2. Investigating HOMO and LUMO Levels Using PBE and B3LYP. Figure 2a,b displays HOMO and LUMO energy levels calculated using the B3LYP hybrid functional, while Figure 2c,d shows analogous levels obtained using the vertical IP and EA (ΔSCF) approach. The bulk band gap values and the GGA−PBE HOMO and LUMO energies of the bulk and (010) surfaces of the dye sensitizers are presented in Table S1 and Figure S1 in the Supporting Information. In this work, we used the *GW*-computed anatase conduction band minimum (CBM)[34] value rather than the experimental value of −4.00 eV,[8] mainly because the flat band potential of anatase in water is slightly more negative than −4.00 eV and recent *GW* calculations have predicted band edges very accurately.[69−71] The anatase CBM is indicated by a black dotted line at −4.12 eV (vs vacuum) for the aqueous medium (see Figure 2). Although the anatase CBM was estimated to be −4.62 eV (vs vacuum) in the gas phase,[34] we only used the value for the aqueous medium for better comparison and figure clarity. The blue dotted line corresponds to the iodide−triiodide (I^-/I^{3-}) redox potential, which is −4.6 eV (vs vacuum).[72] In order to inject electrons efficiently from excited dye molecules into the anatase CBM, the LUMOs of the dye molecules should be less negative than the anatase CBM;[73] in other words, the LUMOs of the dyes must be higher in energy than the anatase CBM. Moreover, to ensure fast dye regeneration following the injection of electrons into the anatase, the HOMOs of the dye molecules must be lower in energy than the I^-/I^{3-} redox potential.[32] All dye molecules in this investigation can effectively inject electrons into the anatase CBM and regenerate, as all LUMOs lie above the anatase CBM and all HOMOs lie below the I^-/I^{3-} redox potential. Both PBE and B3LYP functionals show more negative LUMO and HOMO energies in the aqueous phase than in the gas phase. In addition, PORPC-1 and PORPC-3 have less negative HOMO and LUMO values than PORPC-2 and PORPC-4. According to the literature,[31] a less-negative LUMO value indicates higher dye-molecule stability and better charge-injection ability.

https://dx.doi.org/10.1021/acsomega.0c00870
ACS Omega 2020, 5, 15052−15062

Therefore, these two functionals predict that PORPC-1 and PORPC-3 are better sensitizers than PORPC-2 and PORPC-4; this prediction does not agree with the experimental findings. Furthermore, both functionals predict that PORPC-2 and PORPC-4 have larger gaps than PORPC-1 and PORPC-3 in the gas phase and in water. The smallest band gap is assigned to PORPC-3, regardless of the functional used; however, PBE predicts PORPC-2 to be the dye molecule with the largest band gap. On the other hand, B3LYP predicts that PORPC-4 has the largest band gap in the gas phase, whereas both PORPC-2 and PORPC-4 were calculated to have similar band gaps in water. Clearly, these predictions disagree with the experimental results. The B3LYP functional shows optimal performance with Gaussian type orbital basis set than localized atomic orbitals (LCAO) in DMol.[3] Thus, we believe these erroneous results associated with B3LYP functional attributed to basis set convergence. Generally, PBE functional suffers from electron self-interaction error; hence, band gap and HOMO−LUMO energies are inaccurate.

3.3. IPs and EAs from ΔSCF. The IPs and the EAs of all dye sensitizers calculated using the ΔSCF method show large band gaps in the gas phase due to significantly lower EA values (see Table S1). In other words, the LUMO levels of the dye molecules are compellingly higher in energy than the PBE- and B3LYP-predicted values. With the exception of PORPC-3, all molecules show similar EA (LUMO) energies. As a general trend, the Zn-containing dye molecules have higher IPs than their metal-free counterparts. Piet et al.,[74] reported vertical IPs of several metal-free and Zn porphyrins using experimental ultraviolet photoelectron spectroscopy (UPS) and theoretical methods, including ΔSCF, and found that metal-free *meso*-tetraphenylporphyrin (H2TPP) has a lower vertical IP (6.39 eV UPS, 6.73 eV ΔSCF) than that of Zn *meso*-tetraphenylporphyrin (ZnTPP) (6.42 eV UPS, 6.99 eV ΔSCF).[74] Therefore, our predictions are consistent with experimental observations and the theoretically calculated values. Recently, a large database of dye sensitizers modified with various donor and acceptor groups was theoretically investigated by Ørnsø and co-workers,[53] who predicted that a Zn porphyrin (ZnP) substituted with an ethynyl benzoic acid (EthynPhA) unit at a single meso position has an IP of −6.53 eV (HOMO), EA of −1.57 eV (LUMO), and band gap of 4.96 eV. These values are very similar to those of PORPC-2, despite the presence of two benzoic acid substituents on the Zn-porphyrin framework; PORPC-2 has a band gap of 5 eV, IP of −6.28 eV, and EA of −1.28 eV, which are comparable to those predicted for the EthynPhA-substituted porphyrin. Furthermore, Ørnsø et al.[53] showed that further functional-group substitution at the meso positions of the EthynPhA-substituted ZnP lowered the IPs further. We also observed that two *meso*-phenyl substituents, as in PORPC-3 and PORPC-4, result in IP values that are lower than those of PORPC-1 and PORPC-2. As was also observed by Ørnsø et al.,[53] we did not see any electron-affinity trend in our gas-phase calculations. However, implicit COSMO simulations coupled with the ΔSCF method provide clear IP and EA trends. As predicted in the gas phase, metal-free porphyrins (PORPC-1 and PORPC-3) have lower IPs, and phenyl-group substitutions (PORPC-3 and PORPC-4) further reduce these IPs. On the other hand, metal-free porphyrins have higher EAs and phenyl-group substitutions increase the EAs further. Consequently, the less-negative LUMOs (lower EAs) of PORPC-2 and PORPC-4 stabilize these dyes and improve their electron-injection abilities. Assuming that the calculated EAs are close to the oxidation potentials of the dyes, electron-injection values can be quantitatively interpreted as the difference between the anatase CBM and the EAs of the dyes.[73] Hence, the electron-injection abilities of these dyes were determined to be PORPC-2 (−1.57 eV) > PORPC-4 (−1.56 eV) > PORPC-1 (−1.51 eV) > PORPC-3 (−1.3 eV). As a consequence, PORPC-2 and the PORPC-4 are better dye sensitizers, and these dye molecules have similar driving forces for charge injection. However, these results do not correlate with experimental activity trends, perhaps due to the highly hybridized nature of porphyrin-based dyes in addition to the LCAO basis set problem. Thus, molecular orbitals spread through several Kohn−Sham states. For such systems, excited states are poorly represented by the ΔSCF method.

HOMO−LUMO band gap analyses reveal significantly lower band gaps in the aqueous medium than in the gas phase (see Table S1). The lowest band gap is predicted to be associated with PORPC-3, while the highest band gap is assigned to PORPC-2 in both the gas phase and in water. Remarkably, the PORPC-3 and PORPC-4 dye molecules show lower HOMO−LUMO gaps in the gas phase, in agreement with experimental solid-state UV−visible spectroscopy results (see Figure S3 in the Supporting Information), which clearly show high-intensity absorption peaks in the visible region (600−700 nm);[41] however, this trend is different in water, where PORPC-1 and PORPC-3 are assigned the lowest band gap values. These results are attributable to frontier-orbital destabilization due to strong interactions between PORPC-1 and PORPC-3 and the surrounding water. The calculated solvation energies for PORPC-1 (−1.61 eV) and PORPC-3 (−1.66 eV) are higher in magnitude than those of PORPC-2 (−1.50 eV) and PORPC-4 (−1.58 eV). Therefore, we conclude that calculations based solely on gas-phase HOMO−LUMO gaps and absorption spectra may provide misleading predictions of the dye-sensitizer performance.

3.4. Investigating Band Edges and Optical Gaps Using Hybrid PBE0 and TD-DFT. High-level ab initio methods can aid in situations where PBE, B3LYP, and ΔSCF fail to predict experimental results. With this in mind and to establish the activity trend for the dye sensitizers in this study, we subjected them to PBE0 and TD-DFT calculations. HOMO and LUMO energies were obtained from PBE and PBE0 calculations of the bulk and PBE0 calculations of the (010) surface in the gas phase, as illustrated in Figure S2. The PBE0 functional broadens the gap states by pushing the LUMOs to higher energies and the HOMOs to lower energies. The PBE0-predicted bulk band gaps of PORPC-1, PORPC-2, PORPC-3, and PORPC-4 are 3.07, 3.20, 2.99, and 3.12 eV, respectively. As we observed in the PBE and ΔSCF simulations, PBE0 also predicted PORPC-3 to be the dye molecule with the lowest band gap and PORPC-2 to have the highest band gap in both the bulk and surface calculations. The bulk PBE0 calculations predict band-edge values and (010) surface band-edges that are significantly different. These differences are attributable to the accuracies of the starting points for the hybrid-functional simulations. The bulk PBE0 calculations were initiated using PBE-wavefunction data, whereas the surface calculations commenced with converged bulk PBE0 wavefunctions. The lowest singlet excitation energies of the dye molecules in the aqueous environment also show that the lowest optical gap of 1.89 eV corresponds to PORPC-3 and the highest optical gap of 2.05 eV corresponds to PORPC-2, while PORPC-1 and PORPC-4 have optical gaps

https://dx.doi.org/10.1021/acsomega.0c00870
ACS Omega 2020, 5, 15052−15062

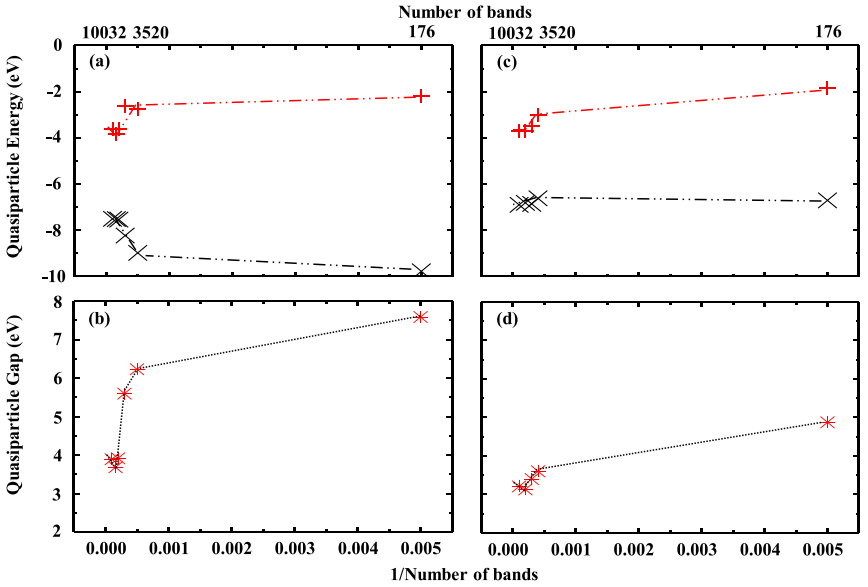

Figure 3. G_0W_0 quasiparticle energies and G_0W_0 band gaps as functions of inverse band number. (a,b) PORPC-4 quasiparticle energies and quasiparticle gaps. (c,d) PORPC-3 quasiparticle energies and quasiparticle gaps. The number of bands is indicated in the top panels. Red crosses in panels (a,c) indicate LUMO levels, while black crosses show HOMO levels calculated by G_0W_0. The red stars in panels (b,d) indicate quasiparticle gaps. All dashed and the dotted lines are for guidance purposes only. Panel (b) shows that the PORPC-4 quasiparticle gap converges very slowly.

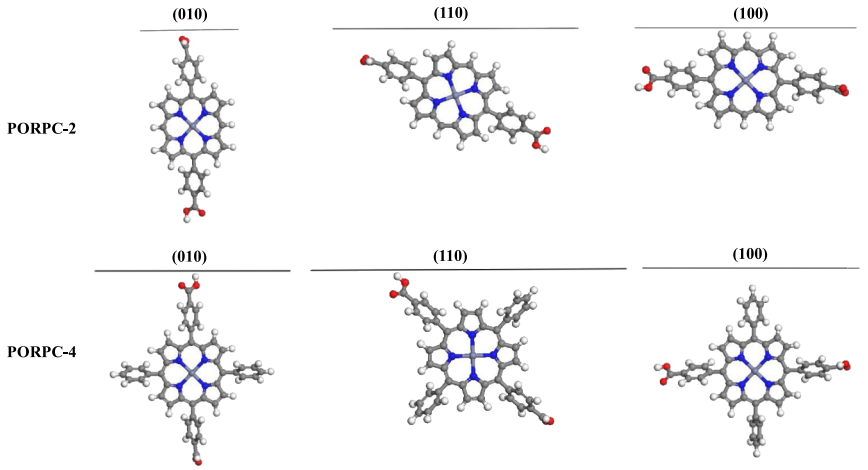

Figure 4. Representative surfaces of PORPC-2 (upper) and PORPC-4 (lower). The black lines indicate surface planes. Color scheme: carbon, hydrogen, nitrogen, oxygen, and zinc are gray, white, blue, red, and light blue, respectively.

of 1.92 and 2.02 eV, respectively. Liu et al.,[66] reported an experimental optical gap of 2.07 eV for a PORPC-4-based MOF; hence, our TD-DFT predicted that the optical gap is in agreement with the experimental value determined for the PORPC-4-based MOF, although TD-DFT represents many-body interaction, which is sensitive to the exchange−correlation functional (partial cancellation of the self-interaction corrections and the electron−hole interaction). However, the TD-DFT results were not explicitly tested for functional dependence to minimize the computational cost. Nevertheless, the PBE0 band gap is sensitive to the amount of Hartree−Fock (HF) exchange used. Here, we particularly employed 30% HF to obtain the above results.

3.5. Investigating Band Edges and Band Gaps Using *GW*.

G_0W_0 single-shot calculations are regarded to be among the best methods available for understanding the band-edge positions of semiconductors.[34] With this in mind, we first evaluated the HOMO and LUMO energy levels of PORPC-1 and PORPC-2 supercells using 400 eV PAW cutoffs and 200 eV *GW* basis-set cutoffs, with 176−10,032 bands. Surprisingly, the HOMO−LUMO gaps of the PORPC-1 and the PORPC-2 supercells converged to the PBE0-predicted values of 3.07 and 3.2 eV, respectively. On the contrary, PORPC-3 and PORPC-4 converged poorly due to the limitations of the *GW* basis-set cut-off used; consequently, maximum *GW* basis-set cutoffs of 100 eV were used with 400 eV PAW cutoffs for the PORPC-3 and PORPC-4 supercells. Figure 3 shows how the HOMO and LUMO energies and the HOMO−LUMO gaps slowly converged. The HOMO values converge much better with a higher number of bands than the LUMO values for both dye molecules. As a consequence, the LUMO values are less reliable than the HOMO values. Therefore, this problem was solved by fitting the last four HOMO data points to the equation: $E_{nk}^{QP} = a/N_{band} + b$, as described in the literature;[65] the PBE0 bulk band gap values were then added to recover the LUMO levels. In the above equation, E_{nk}^{QP} is the quasiparticle

https://dx.doi.org/10.1021/acsomega.0c00870
ACS Omega 2020, 5, 15052−15062

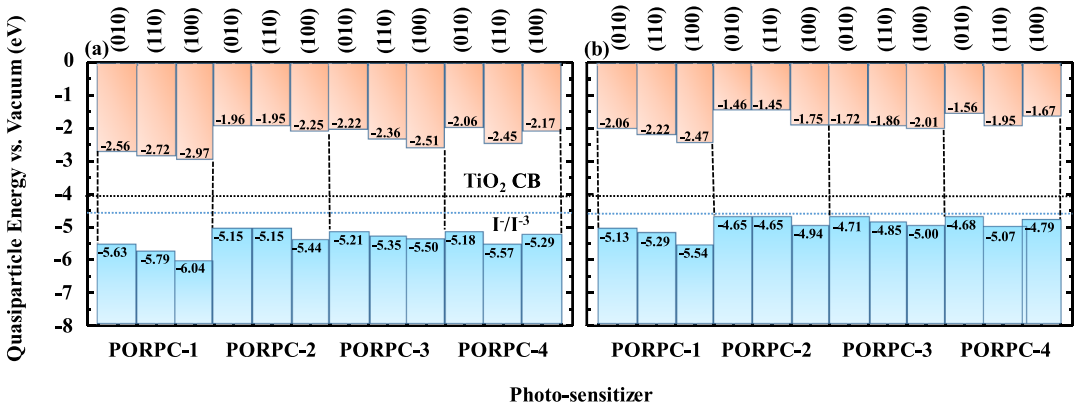

Figure 5. Quasiparticle HOMO−LUMO energy levels relative to the vacuum for all dye molecules investigated in this study. (a) Gas-phase relative quasiparticle energies and (b) energy levels corrected for the aqueous environment. LUMO levels are shown in orange and HOMO levels are shown in blue. The values of the HOMO and LUMO levels are provided for ease of comparison. Vertical dashed lines separate the various sensitizers. The surface orientations of each dye molecule are indicated at the top of the figure.

energy, N_{band} is the number of bands, a is the gradient of the slope, and b is the intercept of the slope. Figure 3b,d shows that the band gap energies begin to diverge at 10,032 bands due to LUMO divergence. Hence, we removed the values corresponding to the LUMOs and extrapolated both HOMO and LUMO levels to the infinite-band limit; that way the recovered PBE0 band gap values support our initial approach. In fact, we used the above-mentioned extrapolation equation to predict the HOMO and LUMO energies of all dye supercells. Nonetheless, this approach is unable to yield more-relevant results under aqueous conditions.

As proposed by Stevanović[34] et al. and Kang[65] et al., we calculated the gas-phase HOMO and LUMO energies of the dye supercells with respect to surface orientation and predicted the energy-level shifts of the dye sensitizers in water by shifting the values by 0.5 eV toward the vacuum level. These dye molecules were not explicitly tested for their lowest-energy surfaces; however, Motoyama and co-workers[75] experimentally verified that the (110) surface is the most stable surface of 5,10,15,20-tetrakis (4-carboxyphenyl)porphyrin (H2TCPP). Because this structure is quite similar to that of the PORPC-3 metal-free porphyrin, we assumed that PORPC-3 and PORPC-4 also have (110) lowest-energy surfaces. In addition, Min et al.[39] adsorbed the (010) surface of a dye sensitizer onto the (101) anatase surface. To provide better understanding, we also chose the (100) surface orientation in addition to the two mentioned above. Hence, three surface orientations were chosen for each surface supercell slab, with the orientations [(010), (110), and (100)] displayed in Figure 4 using the PORPC-2 and PORPC-4 structures as representative examples. Slab calculations were used to test the thickness of the vacuum region, from 10 to 25 and 35 Å, with 25 Å found to be sufficient. Slab thickness was also checked from 10 to 20 and 30 Å. Thick slabs (25 Å) are required for the (010) and (100) surfaces, but thinner slabs (15 Å) are sufficient for the (110) surfaces. Using the surface-orientation-dependent potential step $\Delta V(hkl)$, we determined the HOMO and the LUMO positions of all dye molecules with respect to the vacuum level for the (010), (110), and (100) surfaces, the results of which are shown in Figure 5. Figure 5a shows gas-phase HOMO and LUMO energy levels with respect to the vacuum level, while Figure 5b reveals HOMO and LUMO shift in an aqueous environment. This recipe serves to correlate the HOMO and the LUMO energies with respect to the vacuum rather than the Coulomb potential. Consequently, these results are more universally comparable with experimental data, as the data from commonly used experimental methods, such as photoemission spectroscopy, are measured with respect to the vacuum level.[34] Furthermore, due to the 0.5 eV shift, the HOMO and the LUMO levels of the dye sensitizers can be conveniently compared with those determined electrochemically.

More-recent research found that metal oxide photocatalysts with magnetic ground states have HOMO−LUMO levels that are shifted away from the vacuum (downshifted), while those with nonmagnetic ground states have their levels shifted toward the vacuum (upshifted) in an aqueous medium.[76] Therefore, the 0.5 eV upward shifts of the HOMO and the LUMO levels toward the vacuum in an aqueous medium are justifiable because the dye sensitizers investigated in this study have nonmagnetic ground states. Noticeably, all dye surface orientations are suitable for adsorption onto the anatase (101) surface. Zn-porphyrin-functionalized sensitizers with EthynPhA anchor groups have experimentally determined HOMO levels that range between −5.25 and −5.60 eV in a vacuum.[53] Our calculations provide HOMO levels between −5.15 and −5.57 eV for Zn-porphyrin-functionalized sensitizers in the gas phase, which qualitatively agree with the experimental HOMO levels of the above-mentioned EthynPhA-containing Zn-porphyrin-functionalized sensitizers.[53] The (010) surface band-edge values in Figure 5 reveal that PORPC-2 and PORPC-4 are clearly the most stable and exhibit the highest charge-injection abilities to the anatase CBM. Based on the *GW*-calculated charge-injection abilities, the dye sensitizers are ranked in the following order: −2.66 eV (PORPC-2) > −2.56 eV (POPRC-4) > −2.40 eV (PORPC-3) > −2.06 eV (POPRC-1); however, the experimentally determined activity trend is PORPC-4 > PORPC-2 > PORPC-3 > PORPC-1.[39] We believe the difference between experimental and theoretical results attributed to the single-particle nature of the G_0W_0 method. In addition, all of the methods (except TD-DFT) that are employed in this investigation do not represent many-body interactions. Lack of many-body interaction in single-particle approaches hinders accurate prediction of the dye-sensitizers performance trends. However, due to the higher computational cost associated with many-body methods such as *GW*-BSE (Bethe−Salpeter), we used a dye-aggregation

https://dx.doi.org/10.1021/acsomega.0c00870
ACS Omega 2020, 5, 15052−15062

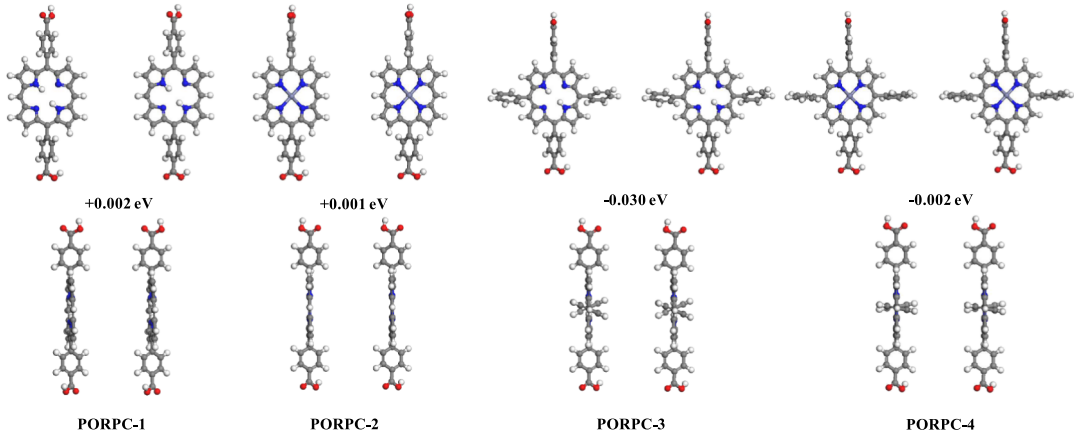

Figure 6. Edge-to-edge (*J*-type) and a face-to-face (*H*-type) aggregation assembly patterns of the dye molecules in the aqueous environment. *J*-aggregation patterns (upper) and *H*-aggregation patterns (lower). PORPC-1 and PORPC-2 prefer to be *H*-aggregated, whereas PORPC-3 and PORPC-4 preferred *J*-aggregation assemblies. Negative energies indicate that the *J*-aggregation configurations are more stable. Color scheme: carbon, hydrogen, nitrogen, oxygen, and zinc are gray, white, blue, red, and light blue, respectively.

assembly pattern to predict dye-sensitizer performance trend in synergy with the G_0W_0 approach.

3.6. Dye-Molecule Aggregation. The aggregation of dye molecules in the aqueous medium is another useful limitation of charge-carrier transport. Dye molecules that aggregate in a "face-to-face" or an "edge-to-edge" manner are referred to as *H* or *J*-aggregates, respectively.[38] Verma and Ghosh[38] proposed that *J*-aggregates facilitate charge funneling thus, enhance long-range charge mobility. Moreover, these authors claimed that electronic transitions from the lowest exciton to the ground state are forbidden in *H*-aggregates, which limits charge-carrier mobility over long distances.[38] With this in mind, we carefully examined the *H*- and *J*-aggregate behavior of the dye molecules under investigation and observed that PORPC-1 and PORPC-2 prefer to be *H*-aggregated rather than *J*-aggregated. On the other hand, PORPC-3 and PORPC-4 prefer the *J*-aggregation assembly over *H*-aggregation. Figure 6 displays the *H*- and *J*-aggregation orientations and their energy differences. Although PORPC-4 has a slightly lower charge-injection ability, *J*-aggregation in the aqueous medium may provide effective long-distance charge transport that enhances its photocatalytic activity. Moreover, PORPC-3 has a much lower charge-injection ability than that of PORPC-2; consequently, it exhibits inferior photocatalytic performance even though it is assembled in a *J*-aggregated manner. As both PORPC-3 and PORPC-4 prefer *J*-aggregation, we conclude that phenyl substitution plays a crucial role in determining the aggregation-assembly pattern in the aqueous medium. Surprisingly, interconverting the *H*- and *J*-aggregates requires very little energy. As Verma and Ghosh[38] suggested, these aggregated forms are easily manipulated by adjusting the pH, temperature, the surrounding environment, or epitaxial-growth conditions. Therefore, both the HOMO−LUMO energy levels and the aggregation patterns in the aqueous medium are important and need to be accurately predicted. Taken together, HOMO and LUMO energy-level studies and the aggregation-assembly-pattern investigations allow us to establish the following photocatalytic activity ordering: PORPC-4 > PORPC-2 > PORPC-3 > PORPC-1, which is in good agreement with the experimental findings.

4. CONCLUSIONS

We used computational methods to investigate two metal-free and two Zn porphyrins functionalized with benzoic acid and phenyl groups at their meso positions for use in solar-energy-driven water-purification applications. Several DFT functionals, namely, PBE, B3LYP, and PBE0 were used, with further calculations performed using ΔSCF, TD-DFT with RPA, and G_0W_0 methods. Interestingly, single-molecule studies using the DMol3 software and the PBE and B3LYP functionals incorrectly order dye-sensitizer activities in both gas-phase and aqueous environments. The ΔSCF method under aqueous conditions accurately predicts the most-active dye sensitizers for water purification, although the order of activity was not accurately predicted for all the molecules.

The lowest first-optical excitations of the dye molecules in water were calculated using TD-DFT; their ΔSCF band gap values in water, PBE0 HOMO−LUMO gaps, and G_0W_0 band gaps confirmed that PORPC-2 has the highest HOMO−LUMO band gap while PORPC-3 has the lowest, with band gaps ascending in the order: PORPC-3 < PORPC-1 < PORPC-4 < PORPC-2. Clearly, the band gap-based approach erroneously concludes that the most-active dye molecules are PORPC-3 and PORPC-1. Solid-state UV−visible spectroscopy also falsely concludes that PORPC-3 and PORPC-4 are the most-active dye sensitizers. However, the ΔSCF and the TD-DFT methods coupled with the implicit solvation model provide more-reliable results. The G_0W_0 method correctly predicts that PORPC-2 and PROPC-4 are the best candidate materials for water purification. Using an aqueous environment (0.5 eV shift) in the G_0W_0 method enables the dye regeneration process to be assessed. Therefore, the effect of the aqueous environment needs to be accounted for in computational studies in order to understand dye-sensitizer performance for water-purification applications.

Nevertheless, HOMO and LUMO energy levels alone are not sufficient to properly establish activity trends using computational methods. The G_0W_0 method also predicted that PORPC-2 is more active than PORPC-4. This is attributed to the single-particle nature of the methods, which are used in this study. Therefore, we emphasized the importance of many-body effects to predict quantitative and accurate photochemistry of the dye sensitizers. Because of

https://dx.doi.org/10.1021/acsomega.0c00870
ACS Omega 2020, 5, 15052−15062

higher computational cost associated with such methods, we used semiquantitative synergistic approach. Hence, dye-molecule aggregate-assembly patterns are taken into account in order to provide accurate predictions. The PORPC-1 and the PORPC-2 dyes prefer *H*-type aggregation assemblies in the aqueous environment, which limits long-range charge transport due to a lack of charge funneling. On the contrary, PORPC-3 and PORPC-4 prefer *J*-type aggregation; consequently, PROPC-3 and PORPC-4 should be much better sensitizers than PORPC-1 and PORPC-2, due to their higher charge-injection capabilities and long-range carrier-transport abilities. However, the lower LUMO level of PORPC-3 resulted in a charge-injection ability that is lower than that of PORPC-2, which consequently led to inferior solar-energy driven catalytic performance. The results of both the HOMO and the LUMO energy-level studies from G_0W_0 and the aggregation assembly-pattern investigations enable us to establish the following order for the photocatalytic activities: PORPC-4 > PORPC-2 > PORPC-3 > PORPC-1, which is in excellent agreement with the experimental findings. This synergistic approach enables us to overcome the limitations of the single-particle methods and accurately predict dye-sensitizers activity trends. We believe that functionalized dyes for water-purification purposes will be fast-screened in the future by combining energy-level and aggregation studies.

■ ASSOCIATED CONTENT

Supporting Information

The Supporting Information is available free of charge at https://pubs.acs.org/doi/10.1021/acsomega.0c00870.

HOMO−LUMO band gaps (eV) calculated using various methods; GGA-PBE-calculated HOMO and LUMO energy levels for bulk and surface dye molecules; GGA-PBE- and hybrid PBE0-functional-calculated HOMO and LUMO energy levels in the gas phase with periodic boundary conditions; and experimental solid-state UV−visible reflectance spectra of TiO_2-dye-sensitizer complexes and bare TiO_2 (PDF)

■ AUTHOR INFORMATION

Corresponding Author

Seung Geol Lee − *Department of Organic Material Science and Engineering, Pusan National University, Busan 46241, Republic of Korea;* orcid.org/0000-0001-7965-7387; Email: seunggeol.lee@pusan.ac.kr

Authors

Jeffrey Roshan De Lile − *Department of Organic Material Science and Engineering, Pusan National University, Busan 46241, Republic of Korea*

Sung Gu Kang − *School of Chemical Engineering, University of Ulsan, Ulsan 44610, Republic of Korea;* orcid.org/0000-0003-1112-7077

Young-A Son − *Department of Advanced Organic Materials Engineering, Chungnam National University, Daejeon 305-764, Republic of Korea;* orcid.org/0000-0001-5143-5926

Complete contact information is available at: https://pubs.acs.org/10.1021/acsomega.0c00870

Notes

The authors declare no competing financial interest.

■ ACKNOWLEDGMENTS

This study was supported by the Basic Science Research Program through the National Research Foundation of Korea (NRF) funded by the Ministry of Science, ICT and Future Planning (nos. 2016M1A2A2937151 and 2017R1E1A1A01074266). The authors thank Dr. Ashen Lankathilaka for his help with visual analysis.

■ REFERENCES

(1) Hoekstra, A. Y.; Chapagain, A. K. Water footprints of nations: water use by people as a function of their consumption pattern. *Integrated Assessment of Water Resources and Global Change*; Springer, 2006; pp 35−48.

(2) Peters, G. P.; Weber, C. L.; Guan, D.; Hubacek, K. China's growing CO2 emissions a race between increasing consumption and efficiency gains. *Environ. Sci. Technol.* **2007**, *41*, 5939−5944.

(3) Delgado, C.; Rosegrant, M.; Steinfeld, H.; Ehui, S.; Courbois, C. Livestock to 2020: The next food revolution. *Outlook Agric.* **2001**, *30*, 27−29.

(4) Shaner, M. R.; Atwater, H. A.; Lewis, N. S.; McFarland, E. W. A comparative technoeconomic analysis of renewable hydrogen production using solar energy. *Energy Environ. Sci.* **2016**, *9*, 2354−2371.

(5) Crabtree, G. W.; Lewis, N. S. Solar energy conversion. *Phys. Today* **2007**, *60*, 37−42.

(6) Zhu, S.; Wang, D. Photocatalysis: basic principles, diverse forms of implementations and emerging scientific opportunities. *Adv. Energy Mater.* **2017**, *7*, 1700841.

(7) O'regan, B.; Grätzel, M. A low-cost, high-efficiency solar cell based on dye-sensitized colloidal TiO2 films. *Nature* **1991**, *353*, 737.

(8) Grätzel, M. Photoelectrochemical cells. *Nature* **2001**, *414*, 338.

(9) Grätzel, M. Conversion of sunlight to electric power by nanocrystalline dye-sensitized solar cells. *J. Photochem. Photobiol. A: Chem.* **2004**, *164*, 3−14.

(10) Sharma, K.; Sharma, V.; Sharma, S. Dye-sensitized solar cells: fundamentals and current status. *Nanoscale Res. Lett.* **2018**, *13*, 381.

(11) Wang, X.; Wang, F.; Sang, Y.; Liu, H. Full-Spectrum Solar-Light-Activated Photocatalysts for Light−Chemical Energy Conversion. *Adv. Energy Mater.* **2017**, *7*, 1700473.

(12) Dong, S.; Feng, J.; Fan, M.; Pi, Y.; Hu, L.; Han, X.; Liu, M.; Sun, J.; Sun, J. Recent developments in heterogeneous photocatalytic water treatment using visible light-responsive photocatalysts: a review. *RSC Adv.* **2015**, *5*, 14610−14630.

(13) Hoffmann, M. R.; Martin, S. T.; Choi, W.; Bahnemann, D. W. Environmental applications of semiconductor photocatalysis. *Chem. Rev.* **1995**, *95*, 69−96.

(14) Di Paola, A.; García-López, E.; Marcì, G.; Palmisano, L. A survey of photocatalytic materials for environmental remediation. *J. Hazard. Mater.* **2012**, *211−212*, 3−29.

(15) Linsebigler, A. L.; Lu, G.; Yates, J. T., Jr. Photocatalysis on TiO2 surfaces: principles, mechanisms, and selected results. *Chem. Rev.* **1995**, *95*, 735−758.

(16) Kakuma, Y.; Nosaka, A. Y.; Nosaka, Y. Difference in TiO 2 photocatalytic mechanism between rutile and anatase studied by the detection of active oxygen and surface species in water. *Phys. Chem. Chem. Phys.* **2015**, *17*, 18691−18698.

(17) Khan, S. U. M.; Al-Shahry, M.; Ingler, W. B. Efficient photochemical water splitting by a chemically modified n-TiO2. *Science* **2002**, *297*, 2243−2245.

(18) Devi, L. G.; Kumar, S. G. Influence of physicochemical−electronic properties of transition metal ion doped polycrystalline titania on the photocatalytic degradation of Indigo Carmine and 4-nitrophenol under UV/solar light. *Appl. Surf. Sci.* **2011**, *257*, 2779−2790.

(19) Mirkovic, T.; Ostroumov, E. E.; Anna, J. M.; Van Grondelle, R.; Govindjee, G. D.; Scholes, G. D. Light absorption and energy transfer in the antenna complexes of photosynthetic organisms. *Chem. Rev.* **2016**, *117*, 249−293.

(20) Janssen, P. J.; Lambreva, M. D.; Plumeré, N.; Bartolucci, C.; Antonacci, A.; Buonasera, K.; Frese, R. N.; Scognamiglio, V.; Rea, G. Photosynthesis at the forefront of a sustainable life. *Front. Chem.* **2014**, *2*, 36.
(21) Panitchayangkoon, G.; Hayes, D.; Fransted, K. A.; Caram, J. R.; Harel, E.; Wen, J.; Blankenship, R. E.; Engel, G. S. Long-lived quantum coherence in photosynthetic complexes at physiological temperature. *Proc. Natl. Acad. Sci. U.S.A.* **2010**, *107*, 12766−12770.
(22) Thorwart, M.; Eckel, J.; Reina, J. H.; Nalbach, P.; Weiss, S. Enhanced quantum entanglement in the non-Markovian dynamics of biomolecular excitons. *Chem. Phys. Lett.* **2009**, *478*, 234−237.
(23) Ogawa, T.; Obata, F.; Shibata, K. Two pigment proteins in spinach chloroplasts. *Biochim. Biophys. Acta* **1966**, *112*, 223−234.
(24) Bessho, T.; Zakeeruddin, S. M.; Yeh, C.-Y.; Diau, E. W.-G.; Grätzel, M. Highly efficient mesoscopic dye-sensitized solar cells based on donor−acceptor-substituted porphyrins. *Angew. Chem., Int. Ed.* **2010**, *49*, 6646−6649.
(25) Birel, Ö.; Nadeem, S.; Duman, H. Porphyrin-based dye-sensitized solar cells (DSSCs): a review. *J. Fluoresc.* **2017**, *27*, 1075−1085.
(26) Urbani, M.; Grätzel, M.; Nazeeruddin, M. K.; Torres, T. Meso-substituted porphyrins for dye-sensitized solar cells. *Chem. Rev.* **2014**, *114*, 12330−12396.
(27) Pastore, M.; Fantacci, S.; De Angelis, F. Modeling excited states and alignment of energy levels in dye-sensitized solar cells: successes, failures, and challenges. *J. Phys. Chem. C* **2013**, *117*, 3685−3700.
(28) Pastore, M.; Selloni, A.; Fantacci, S.; De Angelis, F. Electronic and Optical Properties of Dye-Sensitized TiO 2 Interfaces. *First Principles Approaches to Spectroscopic Properties of Complex Materials*; Springer, 2014; pp 1−45.
(29) Pastore, M.; Fantacci, S.; De Angelis, F. Ab initio determination of ground and excited state oxidation potentials of organic chromophores for dye-sensitized solar cells. *J. Phys. Chem. C* **2010**, *114*, 22742−22750.
(30) Onida, G.; Reining, L.; Rubio, A. Electronic excitations: density-functional versus many-body Green's-function approaches. *Rev. Mod. Phys.* **2002**, *74*, 601−659.
(31) Santhanamoorthi, N.; Lo, C.-M.; Jiang, J.-C. Molecular design of porphyrins for dye-sensitized solar cells: a DFT/TDDFT study. *J. Phys. Chem. Lett.* **2013**, *4*, 524−530.
(32) Jin, X.; Li, D.; Sun, L.; Wang, C.-L.; Bai, F.-Q. Theoretical design of porphyrin sensitizers with different acceptors for application in dye-sensitized solar cells. *RSC Adv.* **2018**, *8*, 19804−19810.
(33) Monti, S.; Pastore, M.; Li, C.; De Angelis, F.; Carravetta, V. Theoretical investigation of adsorption, dynamics, self-aggregation, and spectroscopic properties of the D102 indoline dye on an anatase (101) substrate. *J. Phys. Chem. C* **2016**, *120*, 2787−2796.
(34) Stevanović, V.; Lany, S.; Ginley, D. S.; Tumas, W.; Zunger, A. Assessing capability of semiconductors to split water using ionization potentials and electron affinities only. *Phys. Chem. Chem. Phys.* **2014**, *16*, 3706−3714.
(35) Klamt, A.; Schüürmann, G. Cosmo - a New Approach to Dielectric Screening in Solvents with Explicit Expressions for the Screening Energy and Its Gradient. *J. Chem. Soc., Perkin Trans. 2* **1993**, 799−805.
(36) Klamt, A. Conductor-Like Screening Model for Real Solvents - a New Approach to the Quantitative Calculation of Solvation Phenomena. *J. Phys. Chem.* **1995**, *99*, 2224−2235.
(37) Klamt, A.; Jonas, V. Treatment of the outlying charge in continuum solvation models. *J. Chem. Phys.* **1996**, *105*, 9972−9981.
(38) Verma, S.; Ghosh, H. N. Exciton Energy and Charge Transfer in Porphyrin Aggregate/Semiconductor (TiO2) Composites. *J. Phys. Chem. Lett.* **2012**, *3*, 1877−1884.
(39) Min, K. S.; Kumar, R. S.; Lee, J. H.; Kim, K. S.; Lee, S. G.; Son, Y.-A. Synthesis of new TiO2/porphyrin-based composites and photocatalytic studies on methylene blue degradation. *Dyes Pigments* **2019**, *160*, 37−47.
(40) Kohn, W.; Sham, L. J. Self-consistent equations including exchange and correlation effects. *Phys. Rev.* **1965**, *140*, A1133.
(41) Hohenberg, P.; Kohn, W. Inhomogeneous electron gas. *Phys. Rev.* **1964**, *136*, B864.
(42) Perdew, J. P.; Burke, K.; Ernzerhof, M. Generalized gradient approximation made simple. *Phys. Rev. Lett.* **1996**, *77*, 3865−3868.
(43) Perdew, J. P.; Burke, K.; Ernzerhof, M. Comment on "Generalized gradient approximation made simple" - Reply. *Phys. Rev. Lett.* **1998**, *80*, 891.
(44) Becke, A. D. A New Mixing of Hartree-Fock and Local Density-Functional Theories. *J. Chem. Phys.* **1993**, *98*, 1372−1377.
(45) Becke, A. D. Density-Functional Exchange-Energy Approximation with Correct Asymptotic-Behavior. *Phys. Rev. A: At., Mol., Opt. Phys.* **1988**, *38*, 3098−3100.
(46) Lee, C.; Yang, W.; Parr, R. G. Development of the Colle-Salvetti Correlation-Energy Formula into a Functional of the Electron-Density. *Phys. Rev. B: Condens. Matter Mater. Phys.* **1988**, *37*, 785−789.
(47) Delley, B. An All-Electron Numerical-Method for Solving the Local Density Functional for Polyatomic-Molecules. *J. Chem. Phys.* **1990**, *92*, 508−517.
(48) Delley, B. From molecules to solids with the DMol(3) approach. *J. Chem. Phys.* **2000**, *113*, 7756−7764.
(49) Delley, B. DMol(3) DFT studies: from molecules and molecular environments to surfaces and solids. *Comp. Mater. Sci.* **2000**, *17*, 122−126.
(50) Delley, B. Time dependent density functional theory with DMol3. *J. Phys.: Condens. Matter* **2010**, *22*, 384208.
(51) *Materials Studio*; BIOVIA: San Diego, CA, USA, 2018.
(52) Delley, B. The conductor-like screening model for polymers and surfaces. *Mol. Simul.* **2006**, *32*, 117−123.
(53) Ørnsø, K. B.; Garcia-Lastra, J. M.; Thygesen, K. S. Computational screening of functionalized zinc porphyrins for dye sensitized solar cells. *Phys. Chem. Chem. Phys.* **2013**, *15*, 19478−19486.
(54) Kresse, G. Dissociation and sticking of H-2 On the Ni(111), (100), and (110) substrate. *Phys. Rev. B: Condens. Matter Mater. Phys.* **2000**, *62*, 8295−8305.
(55) Kresse, G.; Hafner, J. First-principles study of the adsorption of atomic H on Ni (111),(100) and (110). *Surf. Sci.* **2000**, *459*, 287−302.
(56) Hobbs, D.; Kresse, G.; Hafner, J. Fully unconstrained noncollinear magnetism within the projector augmented-wave method. *Phys. Rev. B: Condens. Matter Mater. Phys.* **2000**, *62*, 11556−11570.
(57) Monkhorst, H. J.; Pack, J. D. Special points for Brillouin-zone integrations. *Phys. Rev. B: Solid State* **1976**, *13*, 5188.
(58) Wahl, R.; Vogtenhuber, D.; Kresse, G. SrTiO3 and BaTiO3 revisited using the projector augmented wave method: Performance of hybrid and semilocal functionals. *Phys. Rev. B: Condens. Matter Mater. Phys.* **2008**, *78*, 104116.
(59) De Lile, J. R.; Kang, S. G.; Son, Y.-A.; Lee, S. G. Investigating Polaron Formation in Anatase and Brookite TiO2 by Density Functional Theory with Hybrid-Functional and DFT+ U Methods. *ACS Omega* **2019**, *4*, 8056−8064.
(60) Rohlfing, M.; Louie, S. G. Electron-hole excitations in semiconductors and insulators. *Phys. Rev. Lett.* **1998**, *81*, 2312.
(61) Shishkin, M.; Kresse, G. Implementation and performance of the frequency-dependent G W method within the PAW framework. *Phys. Rev. B: Condens. Matter Mater. Phys.* **2006**, *74*, 035101.
(62) Fuchs, F.; Furthmüller, J.; Bechstedt, F.; Shishkin, M.; Kresse, G. Quasiparticle band structure based on a generalized Kohn-Sham scheme. *Phys. Rev. B: Condens. Matter Mater. Phys.* **2007**, *76*, 115109.
(63) Klimeš, J.; Kaltak, M.; Kresse, G. Predictive G W calculations using plane waves and pseudopotentials. *Phys. Rev. B: Condens. Matter Mater. Phys.* **2014**, *90*, 075125.
(64) Gajdoš, M.; Hummer, K.; Kresse, G.; Furthmüller, J.; Bechstedt, F. Linear optical properties in the projector-augmented wave methodology. *Phys. Rev. B: Condens. Matter Mater. Phys.* **2006**, *73*, 045112.

https://dx.doi.org/10.1021/acsomega.0c00870
ACS Omega 2020, 5, 15052−15062

(65) Kang, Y.; Jeon, S. H.; Cho, Y.; Han, S. Ab initio calculation of ionization potential and electron affinity in solid-state organic semiconductors. *Phys. Rev. B* **2016**, *93*, 035131.
(66) Liu, J.; Zhou, W.; Liu, J.; Fujimori, Y.; Higashino, T.; Imahori, H.; Jiang, X.; Zhao, J.; Sakurai, T.; Hattori, Y.; Matsuda, W.; Seki, S.; Garlapati, S. K.; Dasgupta, S.; Redel, E.; Sun, L.; Wöll, C. A new class of epitaxial porphyrin metal-organic framework thin films with extremely high photocarrier generation efficiency: promising materials for all-solid-state solar cells. *J. Mater. Chem. A* **2016**, *4*, 12739−12747.
(67) Coupry, D. E.; Addicoat, M. A.; Heine, T. Extension of the universal force field for metal−organic frameworks. *J. Chem. Theory Comput.* **2016**, *12*, 5215−5225.
(68) Zhou, W. *Thin Films of Porphyrin-Based Metal-Organic Frameworks Grown by Liquid-Phase Epitaxy*; Karlsruher Institut für Technologie (KIT), 2016.
(69) Shaltaf, R.; Rignanese, G.-M.; Gonze, X.; Giustino, F.; Pasquarello, A. Band offsets at the Si/SiO 2 interface from many-body perturbation theory. *Phys. Rev. Lett.* **2008**, *100*, 186401.
(70) Stevanović, V.; Hartman, K.; Jaramillo, R.; Ramanathan, S.; Buonassisi, T.; Graf, P. Variations of ionization potential and electron affinity as a function of surface orientation: The case of orthorhombic SnS. *Appl. Phys. Lett.* **2014**, *104*, 211603.
(71) Rothenberger, G.; Fitzmaurice, D.; Graetzel, M. Spectroscopy of conduction band electrons in transparent metal oxide semiconductor films: optical determination of the flatband potential of colloidal titanium dioxide films. *J. Phys. Chem.* **1992**, *96*, 5983−5986.
(72) Zhang, G.; Bai, Y.; Li, R.; Shi, D.; Wenger, S.; Zakeeruddin, S. M.; Grätzel, M.; Wang, P. Employ a bisthienothiophene linker to construct an organic chromophore for efficient and stable dye-sensitized solar cells. *Energy Environ. Sci.* **2009**, *2*, 92−95.
(73) Vijay, D.; Varathan, E.; Subramanian, V. Theoretical design of core modified (oxa and thia) porphyrin based organic dyes with bridging thiophene linkers. *J. Mater. Chem. A* **2013**, *1*, 4358−4369.
(74) Piet, D. P.; Danovich, D.; Zuilhof, H.; Sudhölter, E. J. R. Ionization potentials of porphyrins and phthalocyanines. A comparative benchmark study of fast improvements of Koopman's Theorem. *J. Chem. Soc., Perkin Trans. 2* **1999**, 1653−1662.
(75) Motoyama, S.; Makiura, R.; Sakata, O.; Kitagawa, H. Highly crystalline nanofilm by layering of porphyrin metal− organic framework sheets. *J. Am. Chem. Soc.* **2011**, *133*, 5640−5643.
(76) Park, K.-W.; Kolpak, A. M. Optimal methodology for explicit solvation prediction of band edges of transition metal oxide photocatalysts. *Commun. Chem.* **2019**, *2*, 79.

https://dx.doi.org/10.1021/acsomega.0c00870
ACS Omega 2020, 5, 15052−15062